Review

Recent Research Process of Carbon Engineering on Na$_3$V$_2$(PO$_4$)$_3$ for Sodium-Ion Battery Cathodes: A Mini Review

Yaxuan He and Haibo Li *

Ningxia Key Laboratory of Photovoltaic Materials, School of Materials and New Energy, Ningxia University, Yinchuan 750021, China
* Correspondence: lihaibo@nxu.edu.cn

Abstract: Owing to the 3D open framework, excellent structural stability, and high ionic conductivity, NASICON-type compounds are extensively employed as promising cathode materials for sodium-ion batteries (SIBs). Being one of the representative NASICON-type compounds, the Na$_3$V$_2$(PO$_4$)$_3$ delivers high theoretical capacity with an operating voltage exceeding 3.3 V, enabling it to be a good candidate for SIBs. Unfortunately, the Na$_3$V$_2$(PO$_4$)$_3$ suffers from low electronic conductivity. In this work, we briefly review the recent research progress on novel carbon engineering strategies to enhance the electronic conductivity of Na$_3$V$_2$(PO$_4$)$_3$. Moreover, we will point out the issues relating to the development of NASICON cathode materials and put forward some suggestions.

Keywords: sodium ion batteries; Na$_3$V$_2$(PO$_4$)$_3$; carbon materials; conductivity

1. Introduction

Lithium-ion batteries (LIBs) are widely used in high-energy storage fields, such as electric vehicles, communications, and smart electronics [1–4]. However, the development of LIBs is threatened by the limited lithium resources where the earth's crust content of lithium is only 0.0065% [5–7]. Therefore, it is crucial to develop alternatives to replace LIBs in the future. Compared to lithium, the sodium reserve is abundant in the earth's crust (2.8%) and sea (10.77g/kg) [8], and Na exhibits similar properties as Li since they all settle in group IA of the periodic tables. As realized in Table 1, Na also has a low standard electrode potential of −2.71 V, which is just slightly higher than Li (−3.04 V) [9–14]. As a result, SIBs have similar working principles to LIBs in that Na$^+$ can reversibly shuttle between cathode and anode, causing a voltage potential difference that leads to the mutual conversion of electrical and chemical energy. However, the large ionic radius (1.02 Å) and atomic mass (22.99 g/mol) of Na$^+$ result in low theoretical capacity, high resistance, and sluggish transport kinetics during the Na$^+$ insertion/de-insertion [15–18]. Thus, some traditional electrode materials applied for LIBs are not suitable in SIBs directly, such as the extensively used LiCoO$_2$ cathode and the graphite anode. Therefore, it is significant to explore SIB electrode materials with exceptional Na$^+$ insertion/de-insertion kinetics and Na$^+$ storage performance. Associating with electrochemical batteries, cathode materials as an essential component of batteries, make great contributions to strengthening electrochemical performance. This is because the inherent crystal structure of the cathode materials determines the electrochemical behavior of SIBs, including redox potential, the number of electron transfers, and structural stability. The main cathode materials adapted to SIBs can be classified into three types: (1) stratified material [19–22], (2) polyanionic compounds [23–26], and (3) macromolecule polymer material [27–31]. Further, Table 2 shows the performance of different cathode materials for SIBs.

Table 1. The comparison of sodium and lithium.

Metal	Na	Li
Atoms radius/Å	1.86	1.52
Ionic radius/Å	1.02	0.76
Standard electrode potential/V	−2.71	−3.04
Earth crust abundance	2.8%	0.0065%
Theoretical specific capacity/(mah/g)	1166	3862

Table 2. The comparison of performance among different cathodes for SIBs.

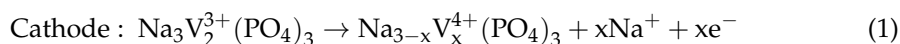| Materials	Voltage	Reversible Capacity	Rate Performance	Ref.
$NaMnO_2$	2.59 V	C/30, 149 mAh/g	C/10, 144 mAh/g	[32]
$Na_{0.5}Co_{0.5}Mn_{0.5}O_2$	2.8 V	C/2, 141 mAh/g	5 C, 80 mAh/g	[33]
$NaNi_{0.5}Mn_{0.5}O_2$	>2.5 V	C/50, 125 mAh/g	C/30, 100 mAh/g	[34]
$NaAl_{0.1}Mn_{0.9}O_2$	2.56 V	-	C/10, 145 mAh/g	[35]
$Na_{0.66}Ni_{0.33}Mn_{0.62}Mo_{0.05}O_2$	3.25 V	34 mA/g, 125 mAh/g	1 C, 112 mAh/g	[36]
$NaNi_{0.60}Fe_{0.25}Mn_{0.15}O_2$	3.1 V	C/2, 190 mAh/g	2 C, 134 mAh/g	[37]
$Na_{0.7}CoO_2$	2.8 V	0.04 C, 125 mAh/g	16 C, 64 mAh/g	[38]
$Na_{1.92}Fe[Fe(CN)_6]$	3.2 V	C/10, 157 mAh/g	10 C, 145 mAh/g	[39]
$NaFeO_2$	3.4 V	10 mA/g, 94 mAh/g	-	[40]
$Na_{0.67}Fe_{0.425}Mn_{0.425}Mg_{0.15}O_2$	3.6 V	C/10, 146.6 mAh/g	2 C, 58.4 mAh/g	[41]
$Na_2PDHBQS/RGO$	1.4 V	C/10, 228 mAh/g	4 C, 147 mAh/g	[42]
$Na_2C_6O_6$	2.1 V	C/10, 190 mAh/g	10 C, 95 mAh/g	[43]
CNF-GC-NVP	3.4 V	1 C, 123.77 mAh/g	60 C, 95.59 mAh/g	[44]
$Na_2MnP_2O_7$	3.6 V	C/10, 94 mAh/g	10 C, 55 mAh/g	[45]

Polyanionic compounds have been regarded as one of the most attractive cathode materials due to their Na^+ superionic conductor (NASICON) structure and adjustable redox potential [46–50]. The general formula of NASICON-type compounds is described as $A_xM_2(XO_4)_3$ (A = Na, Li, Fe, etc., M = V, Ti, Fe, Tr or Nb, etc., X = P or S and x = 0–4). The NASICON-type $A_xM_2(XO_4)_3$ is constructed by corner-shared MO_6 and polyhedral XO_4 groups, which provide convenient Na^+ diffusion channels [51]. The open 3D framework and large pore channels make the polyanionic compounds possess high Na^+ conductivity and long-term structure stability [52–57]. Among various NASICON-type $A_xM_2(XO_4)_3$, the $Na_3V_2(PO_4)_3$ (NVP) cathode offers a high Na^+ storage capacity of 117 mAh/g with high structural stability. However, the separation of TiO_6 octahedrons leads to poor electronic conductivity, which further influence rate capability and cyclic stability [58–63]. In order to overcome these problems, many advanced strategies have been proposed. The typical approaches involve particle nano-sizing, doping, and coating with carbons, including graphene, carbon black, and carbon nanotubes (CNTs), etc. [64–69].

In this review, we initially analyze the structure−performance relationship of NVP for SIBs and then briefly summarize the research process of the carbon coating approaches to modify the NVP. Significantly, the modifications that can improve the conductivity of NVP by carbon coating strategies are emphatically introduced. Moreover, the challenges and future development direction of the NASICON-type cathode have been prospected. It is expected that this work will be a meaningful reference to guide the design of high-performance NVP cathodes for SIBs.

2. The Structure and Properties of NVP

Vanadium has rich oxidation valence states, which contain V^{5+}, V^{4+}, V^{3+}, and V^{2+}. Theoretically, the NVP cathode reveals a high capacity of 117 mAh/g because of the conversion of V^{3+}/V^{4+} [70,71]. Meanwhile, its highly open framework enables the creation of 3D diffusion channels and large migration gaps for Na^+, and the diffusion coefficient of Na^+ can reach 10^{-10} cm^2/s [72,73]. Figure 1 shows the crystal structure of $Na_3V_2(PO_4)_3$ generated by VESTA with the monoclinic lattice, and the space group is $P2_1/c$. Besides,

lattice parameters are a = 8.87 Å, b = 9.01 Å, c = 15.44 Å and α = 55.326°, β = 90° and γ = 90°. The structure is composed of VO_6 octahedrons and PO_4 tetrahedrons by sharing an O atom at the vertex. At the same time, two free Na^+ occupy the two oxidation state channels in the lattice. This structure promises excellent structural stability for NVP. For example, Choi et al. [74] studied the thermal stability of the NVP cathode by using TGA-DSC and in situ XRD at various temperatures. Basically, the NVP exhibits no endothermic/exothermic peak and prominent thermal stability even at 450 °C under a deoxidation state, which is ascribed to the high stability of the P-O bond. Moreover, the NVP illuminates the typical redox potentials at 3.4 V vs. Na/Na^{+}, which is higher than that of the majority of cathode materials [75–77]. When employed as a cathode, the cell reaction can be described as:

$$\text{Cathode}: \text{Na}_3\text{V}_2^{3+}(\text{PO}_4)_3 \rightarrow \text{Na}_{3-x}\text{V}_x^{4+}(\text{PO}_4)_3 + x\text{Na}^+ + x\text{e}^- \tag{1}$$

In the charging process, two Na^+ are expelled from the cathode to the anode. Meanwhile, V^{3+} is oxidized to V^{4+} to form $NaV_2(PO_4)_3$, accompanied by the transfer of two electrons. On the contrary, V^{4+} is reduced to V^{3+}, and Na^+ is inserted into the cathode to form NVP.
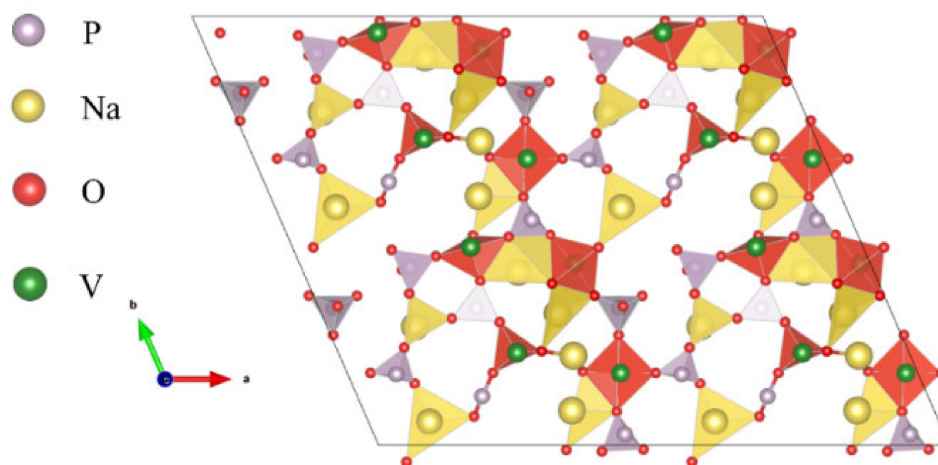

Figure 1. The crystal structure of $Na_3V_2(PO_4)_3$.

3. The Modification Methods to Improve the Conductivity of NVP

Despite the fact that the NVP demonstrates an advance as a cathode for SIBs, the conductivity of NVP is still concerning. Carbon coating engineering is often considered to be one of the most effective methods to improve the electronic conductivity of base materials. It has many advantages, such as low cost, simple operation, and flexibility.

3.1. Graphene

Graphene is a 2D carbon allotrope constituted by sp^2 hybridization. The remaining p orbital electrons in the plane form a large π bond to move freely over graphene, resulting in fast electron mobility and high electrical conductivity. The charge carrier mobility and thermal conductivity of graphene exceed 2×10^5 cm^2/Vs and 3000 W/Mk at an electron density of 2×10^{11} cm^{-2}, respectively. As a result, graphene is employed as a conductive component to composite with NVP by either coating or doping. For example, Rui et al. [78] proposed a 3D NVP-based hybrid cathode, which is composed of NVP@amorphous carbon wrapped by reduced graphene oxide nanosheets (NVP@C@rGO) to achieve efficient charge transfer, as shown in Figure 2a,b. Essentially, the aqueous NVP precursor is mixed with poly (vinylpyrrolidone) (PVP) to construct a nanoporous carbon matrix on NVP nanoparticles. Then, the GO suspension was added to the above solution and followed by performing freeze-drying and heating. In Figure 2c,d, the NVP@C@rGO revealed prominent rate performance; that is, the discharge capacity remained at about 115 mAh/g when the current density varies from 1 to 20 C. Figure 2e shows that the

charge transfer resistance (R_{ct}) of NVP@C@rGO was about 258 Ω, which was much lower than that of NVP@C (639 Ω). Chang et al. [79] synthesized a graphene-bound, binder-free NVP film electrode by simple vacuum-assisted filtration of the NVP and graphene. Figure 2f shows the SEM image of the as-prepared graphene-bound NVP film. Obviously, the 100–300 nm NVP particles are evenly bound to the graphene. Compared with pristine NVP particles, the graphene not only increased the conductivity of the whole electrode but also suppressed the agglomeration of NVP particles. As a result, it exhibited excellent performance under a high rate (Figure 2g). Further, in Figure 2h, the R_{ct} of graphene-bound NVP was significantly smaller than that of pristine NVP, which again confirms that the GO benefits alleviate the electronic conductivity of NVP.
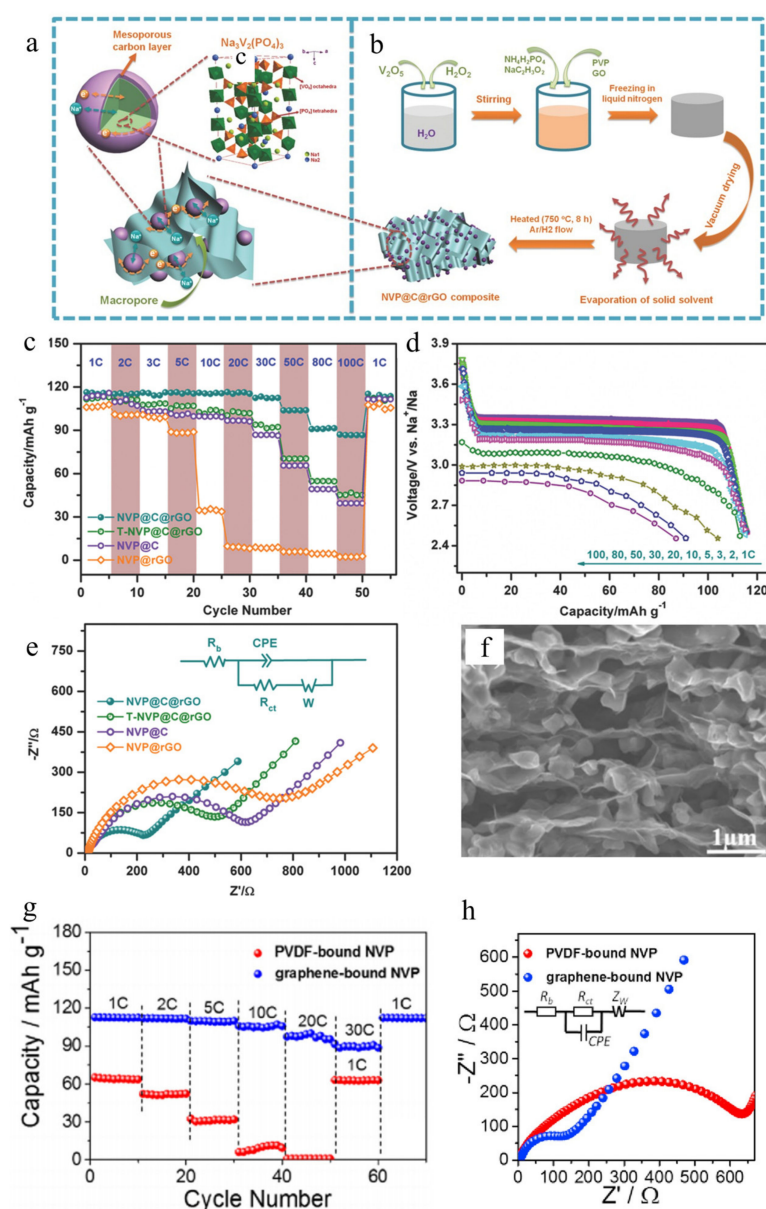

Figure 2. (**a**) Schematic illustration of 3D hierarchical meso- and macroporous NVP@C@rGO cathode with pathways for both electrons and sodium ions, (**b**) schematic illustration of preparing NVP@C@rGO composite, the (**c**) rate performance, (**d**) discharge profiles at various current rates and (**e**) EIS spectra of NVP@C@rGO. Reprinted with permission from Ref. [78]. 2015, Wiley−VCH. The (**f**) SEM image graphene-bound NVP, (**g**) rate performance, and (**h**) EIS spectra of PVDF-bound NVP and graphene-bound NVP. Reprinted with permission from Ref. [79]. 2015, Elsevier.

Besides, Xu et al. [80] prepared NVP/reduced graphene oxide hollow spheres (NVP/rGO HSs) by spray drying and subsequent pyrolysis for Na+ storage (Figure 3a). The SEM and TEM images of NVP/rGO HSs are displayed in Figure 3b,c. The graphene layer was surrounded by a large number of NVP particles, which together formed a hollow sphere (~6 μm). The spherical hollow structure can make full contact between the electrode and electrolyte, and the rGO layer acted as a high-speed electron transferring bridge. Therefore, NVP/rGO HSs exhibited excellent electrochemical performance as well as remarkable rate performance, i.e., the specific discharge capacity was 107.5 mAh/g at 10 C. Further, Xu et al. [81] designed a straightforward and self-assembly approach to fabricate layer-by-layer structured NVP@reduced graphene oxide (NVP@rGO) nanocomposites. In NVP@rGO, the rGO was responsible for offering rapid electron transport. Thus, the NVP@rGO cathode presents superior rate capability (73 mAh/g at 100 C and 41 mAh/g at 200 C).
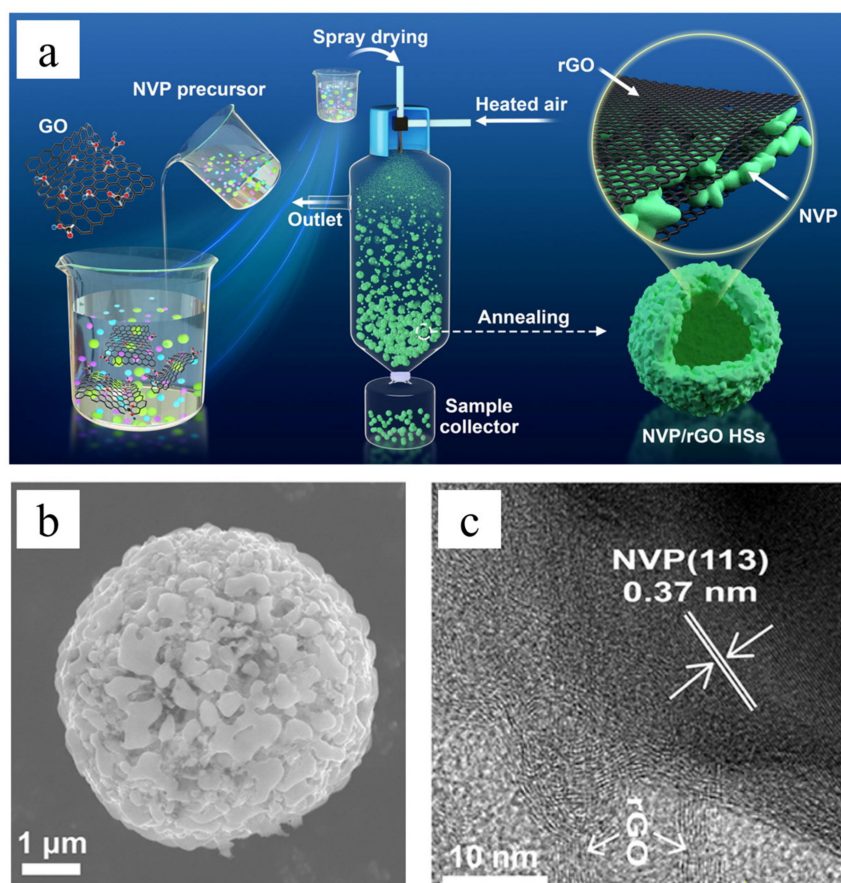

Figure 3. (**a**) Schematic illustration for the fabrication of NVP/rGO HSs, the (**b**) SEM, and (**c**) TEM images of NVP/rGO HSs. Reprinted with permission from Ref. [80]. 2020, Elsevier.

3.2. Carbon Nanotubes

Besides graphene, CNTs are also chosen as conductive blocks to couple with NVP. CNTs can be viewed as coiled from graphene sheets, and the p orbital electrons on CNTs provide more π bonds to produce a strong conjugation effect. As a result, high electrical conductivity is associated with CNTs. For example, Shen et al. [82] developed a simple sol-gel approach to prepare double nano-carbon modified NVP (NVP@C+N@CNTs) to improve the electrochemical characteristic of SIBs, and the corresponding schematic structures of NVP@C+N@CNTs are drawn in Figure 4a. In Figure 4b,c, associating with the TEM image of NVP@C+N@CNTs, it is clear to observe that the NVP is perfectly covered by carbon coatings and simultaneously connected by CNTs to form a 3D network. Such a structure accelerated the electron transport between NVP nanoparticles. In Figure 4d, the specific

discharge capacities of NVP@C+N@CNTs reach 94.5, 94.6, 94.5, 93.6, 93.4, 92.6, 91.5, 92.5, 92.4, and 90.1 mAh/g at 0.2, 0.5, 1, 2, 3, 5, 10, 15, 20, and 30 C, respectively. Even at 70 C, the specific discharge capacity still remained at 70 mAh/g.
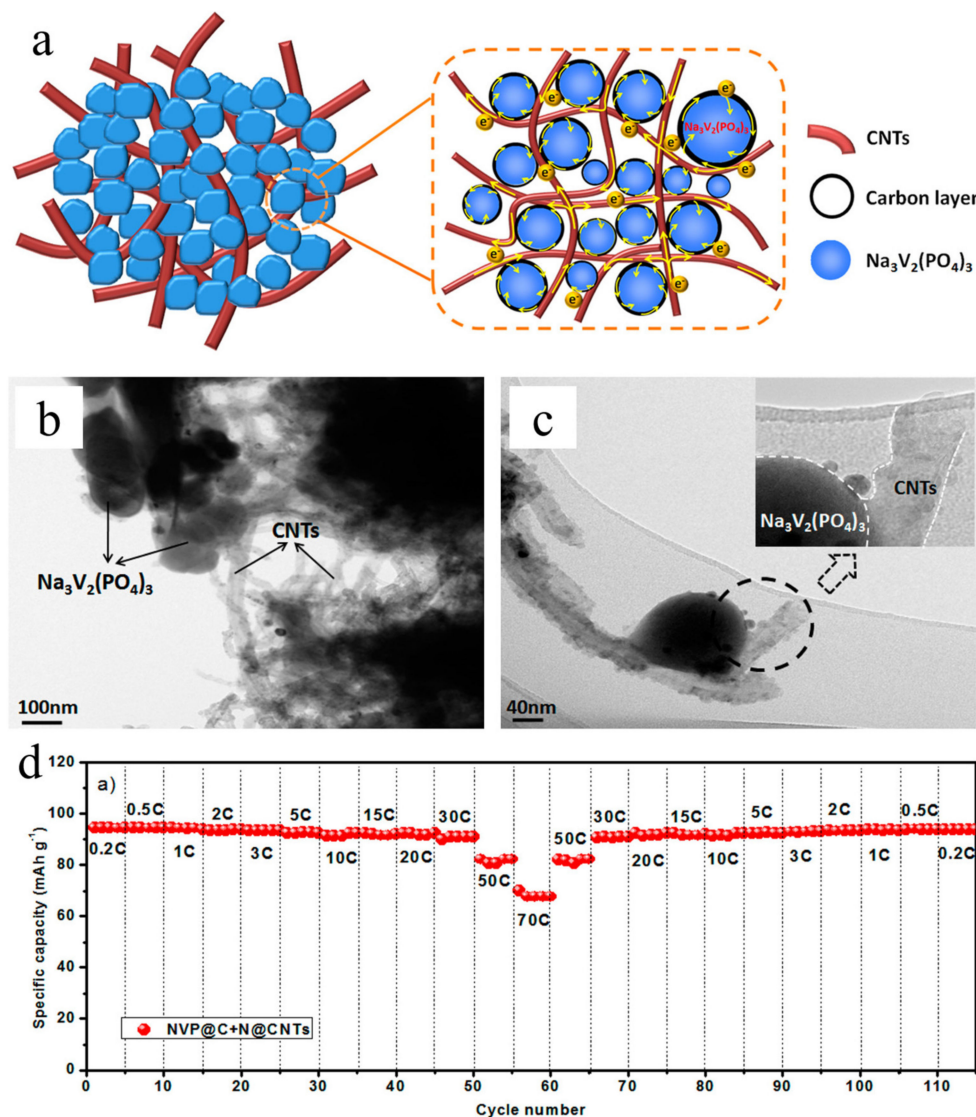

Figure 4. The (**a**) structure, TEM images (**b**,**c**), and (**d**) rate performance of NVP@C+N@CNTs. Reprinted with permission from Ref. [82]. 2016, American Chemical Society.

Chen et al. [83] designed and synthesized a CNT-decorated NVP microsphere via spray drying and a carbothermal reduction approach. The NVP microspheres were embedded by CNTs. Meanwhile, the particles were coated by amorphous carbon layers. Figure 5a–d shows the SEM images of NVP doped with different amounts of CNTs. As the CNTs content increases, fewer NVP particles are observed. This is presumably ascribed to the fact that the CNTs limited the growth of NVP particles. Further, the CNTs and carbon layer can be apparently examined from the TEM images in Figure 5e,f. In this structure, the unique carbon network effectively promoted electron transmission. Most importantly, the incorporation of CNTs significantly enhanced the rate capability (Figure 5g). By comparison with NVP/C, the NVP/C10 illustrated a smaller R_{ct} (225.5 Ω), which is also beneficial to improve the electrochemical properties of the composite electrode (Figure 5h). Beyond these, Sun et al. [84] prepared $Na_3V_2(PO_4)_3$/C@CNTs-WC by a sol-gel method. The C@CNTs formed a conductive framework that accelerated electron transport. At the same time, the

introduction of W^{6+} created abundant cavities on the surface of the NVP. Therefore, the $Na_3V_2(PO_4)_3$/C@CNTs-WC delivers a high capacity of 92.6 mAh/g at a super high rate of 50 C and remains 84.5 mAh/g over 400 cycles.
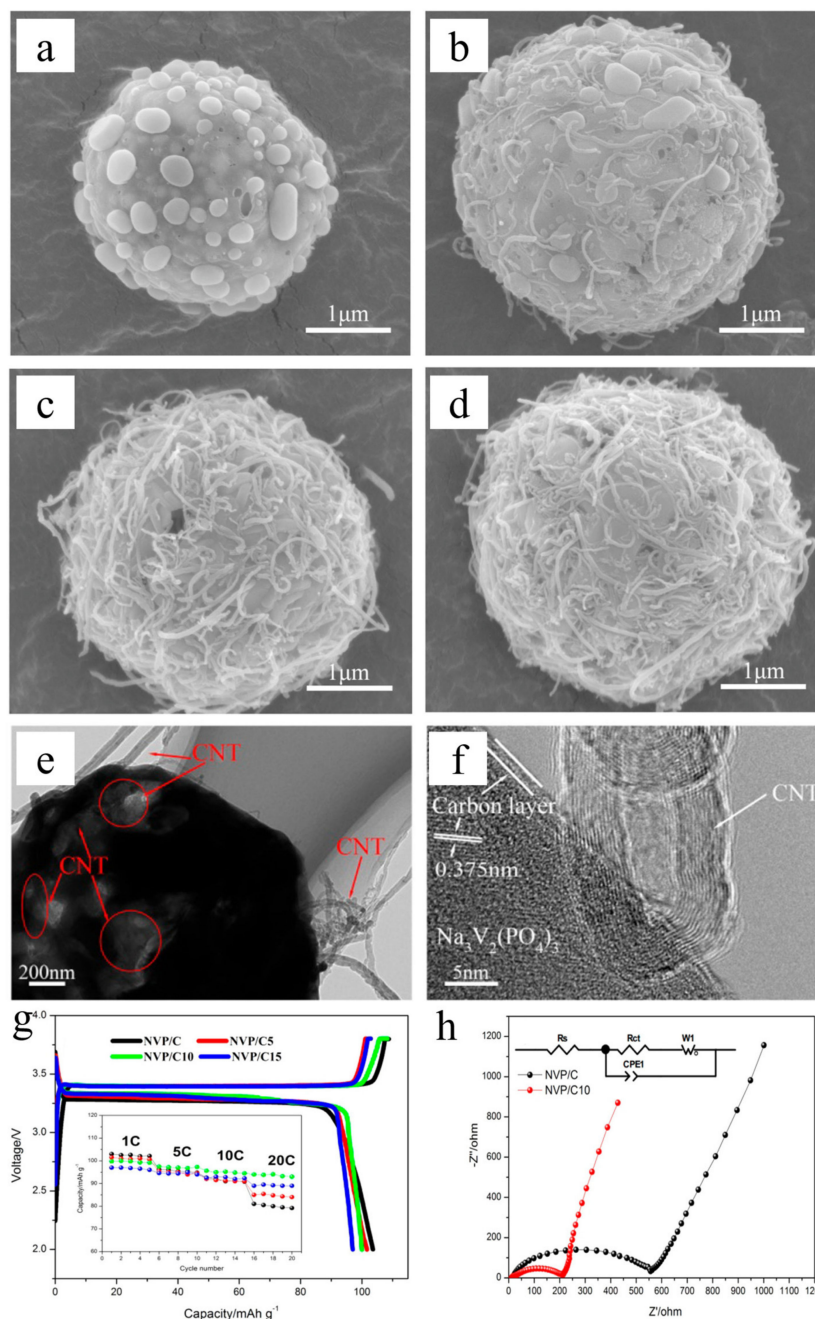

Figure 5. The SEM images of (**a**) NVP/C, (**b**) NVP/C5, (**c**) NVP/C10, and (**d**) NVP/C15, (**e**) TEM and (**f**) HRTEM images of NVP/C10, (**g**) charge/discharge curves of different electrodes at 110 mA/g, the inset is the rate performance, and (**h**) EIS spectra of NVP/C and NVP/C10. Reprinted with permission from Ref. [83]. 2018, American Chemical Society.

3.3. Other Carbon Coatings

In any case, the carbon coating layer (CCL) can inhibit the size of NVP particles during growth. Besides, the CCL acted as a buffer layer to avoid direct contact between the electrolyte and active materials, which helped to weaken the corrosion of the electrolyte over the electrode. Moreover, the CCL is usually amorphous carbon, which has good mechanical properties and stability. For instance, Duan et al. [85] employed a hydrothermal-assisted sol-gel method to

synthesize the core-shelled NVP@C. Notably, there presents a large gap between the as-prepared nano NVP@C particles, which is conducive to urging complete contact between the electrolyte and the NVP@C and thus shortening the Na$^+$ diffusion path. When it was applied for SIBs, the nano NVP@C realized the high specific discharge capacity of 88 mAh/g at 10 C. In the work performed by Li et al. [86], citric acid was used as a carbon resource, reducing agent, and complexing agent. They proposed a method by rheological phase reaction to prepare double carbon-wrapped NVP where amorphous carbon served as a framework together with graphitized carbon, which acted as a conductive network. By this design, the thickness of amorphous carbon is about 5 nm; electrons are quickly transferred to amorphous carbon through graphitized carbon and then transferred to NVP from amorphous carbon, which effectively shortens the transmission path of electrons. Consequently, the NVP@C calcined at 800 °C (NVPC-800) illuminated the best electrochemical performance among all samples calcined at 600, 700, and 900 °C. In Figure 6a,b, relating to the TEM images, the thickness of the disordered carbon layer was ~5 nm, and the graphitized carbon can be clearly observed as well. Figure 6c,d show the cycling performance and EIS spectra of NVPC-800, verifying the prominent cycling stability and low R$_{ct}$. Even the current density increased to 1 C, and the specific discharge capacity of NVPC-800 reached 99.8 mAh/g with more than 98.9% capacity retention after 500 cycles (Figure 6e).
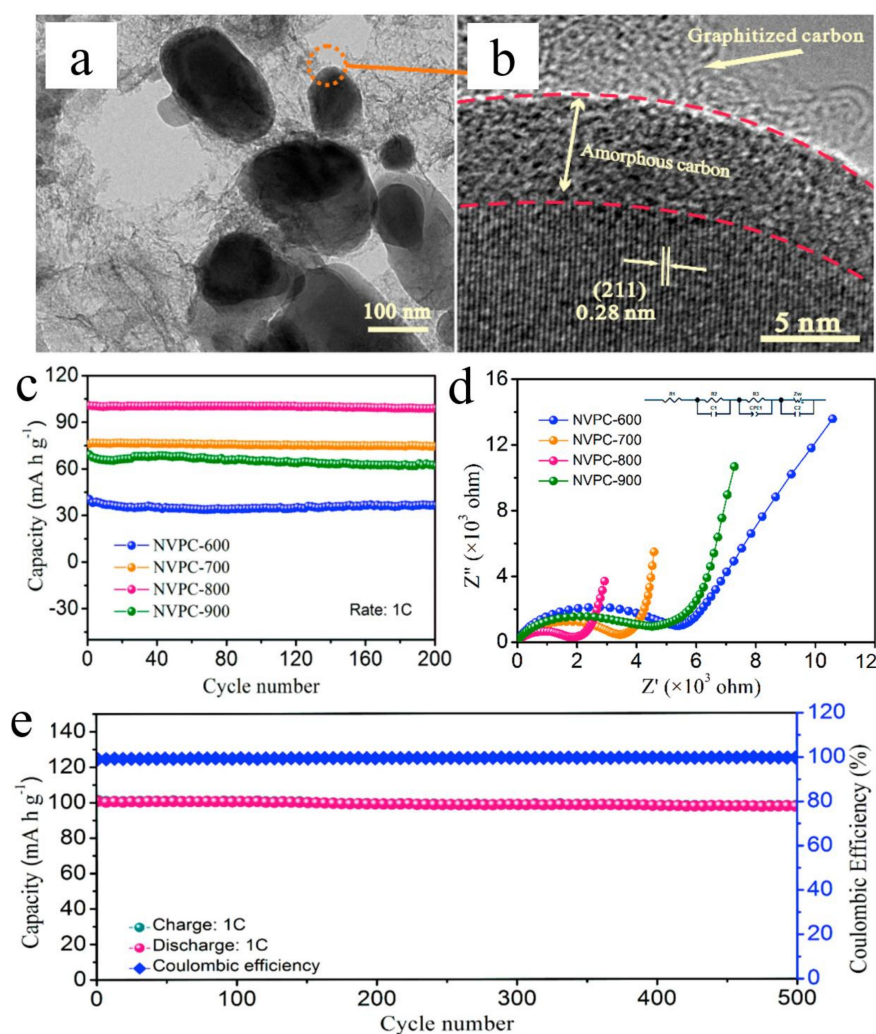

Figure 6. The (**a**) and (**b**) TEM images, (**c**) cycling performance, (**d**) EIS spectra, and (**e**) long-term cycling performance of NVPC-800. Reprinted with permission from Ref. [86]. 2019 Elsevier B.V.

Jiang et al. [87] synthesized carbon-coated nanosized NVP into mesoporous carbons (NVP@C@CMK-3) by a nano-coating technique, as drawn in Figure 7a. It schematically described the reversible electrochemical reactions of the NVP@C nanoconfined within a single carbon pore that the special structure ensured efficient diffusion of electrons and Na^+. In Figure 7b, the NVP@C@CMK-3 reveals the high specific discharge capacity of 115 mAh/g at 110 mA/g, which is much higher than that of pure NVP (83 mAh/g). From Figure 7c, the R_{ct} of the NVP@CMK-3 and NVP@C@CMK-3 is 272 and 207 Ω, respectively, highlighting that the double carbon coating structure facilitates the transportation of Na^+ and e^- and meanwhile generates lower polarization [88,89].
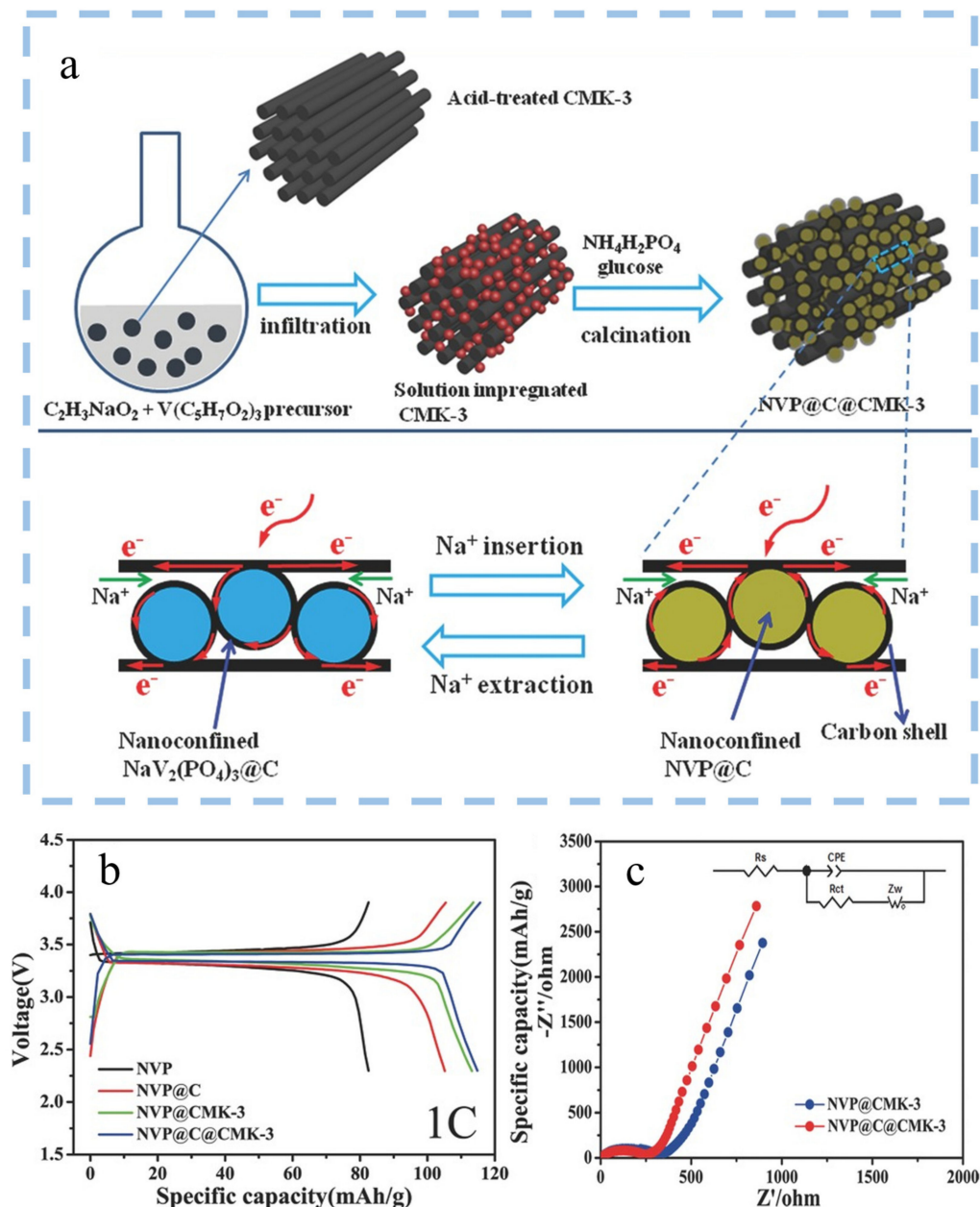

Figure 7. (**a**) Schematical illustrations of fabricating NVP@C@CMK-3 cathode and the electrochemical reactions confined within a single carbon pore, the (**b**) charge/discharge curves and (**c**) EIS spectra of NVP@C@CMK-3. Reprinted with permission from Ref. [87]. 2015, Wiley-VCH.

3.4. Heteroatom Doping

Researchers have found that either anion or cation doping is in favor of improving the intrinsic conductivity of NVP, such as Ag^+, N^{4-}, etc. Basically, ion doping leads to a greater carrier concentration of the doped system over the intrinsic system, which would significantly enhance conductivity. Hong et al. [90] prepared C-Ag co-coated NVP (NVP/C-Ag) and C-coated NVP (NVP/C) by an uncomplicated solid-state method in Figure 8a. From the XRD patterns of NVP/C-Ag in Figure 8b, the typical characteristic peak of silver was captured at 38°. Meanwhile, the diffraction peak of NVP/C-Ag (at about 23.5°) was wider and lower than that of NVP/C, which is attributed to the confined growth of NVP particles due to the presence of the C-Ag layer. Figure 8c displays the TG curves of NVP/C-Ag. When the temperature exceeded 500 °C, the carbon species had completely burned out, and the residual carbon content was about 6%. Figure 8d depicts the charge/discharge curves of NVP/C-Ag at various rates. Upon the current density increases, small changes can be obtained in the specific discharge capacity, featuring excellent rate performance. In Figure 8e, Wang et al. [91] prepared NVP/N-doped carbon composites (NVP-NC) by taking nitrilotrimethylene triphosphonic acid as the multifunctional raw material. Figure 8f shows the SEM image of NVP-NC. It can be seen that NTP particles were encapsulated in an N-doped carbon matrix, which facilitates the rapid transport of Na^+ and electrons. Among all samples, the NVP-NC obtained under 850 °C showed the best Na^+ storage performance, and the corresponding specific discharge capacity was 94.0 mAh/g at 10 C after 600 cycles.
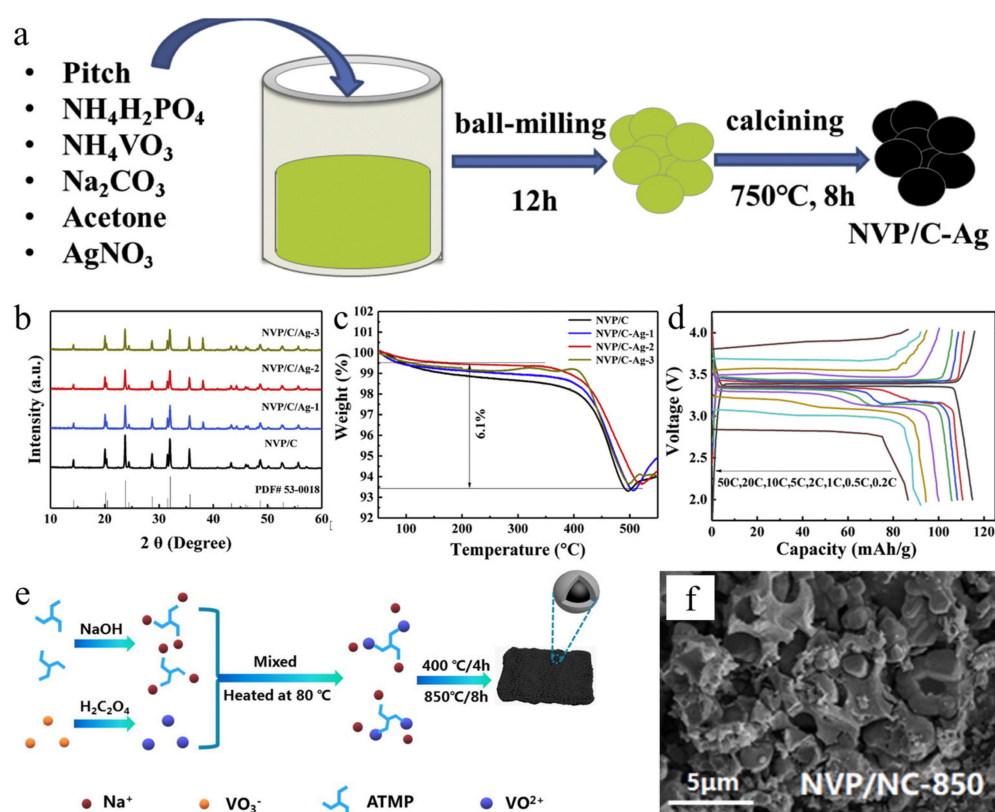

Figure 8. (**a**) Schematic illustration of the formation of NVP/C-Ag, (**b**) XRD patterns, (**c**) TG curves, and (**d**) charge/discharge curves at various current densities of NVP/C-Ag. Reprinted with permission from Ref. [90]. 2020, Elsevier B.V. (**e**) Schematical synthesis of NVP-NC, (**f**) the SEM image of NVP-NC Reprinted with permission from Ref. [91]. 2020, Elsevier B.V.

Jiang et al. [92] designed an (N, S) co-doped graphene (3DPGFs-NS) to accommodate the active materials. Then, the $Na_3V_2(PO_4)_3@C@3DPGFs-NS$ were prepared by a sol-gel method, as presented in Figure 9a. From the SEM image of Figure 9b, the obvious 3D porous structure was

observed. Further, the carbon layer, NVP, and graphene can be clearly differentiated from the TEM image in Figure 9c. The charge/discharge curves of NVP and $Na_3V_2(PO_4)_3$@C@3DPGFs-NS at 110 mA/g are shown in Figure 9d. The $Na_3V_2(PO_4)_3$@C@3DPGFs-NS displays a wider discharge platform, and the curve is smoother, suggesting the outstanding electrical conductivity of (N, S) co-doped 3DPGFs. The specific discharge capacity of $Na_3V_2(PO_4)_3$@C@3DPGFs-NS is 112 mAh/g at 1 C, which is higher than pure NVP (60 mAh/g). Further, the $Na_3V_2(PO_4)_3$@C@3DPGFs-NS reveals excellent cycling ability at 20 C in Figure 9e. Above all, the electrochemical performance of NVP has been improved through the carbon coating and heteroatom doping strategy in Table 3.
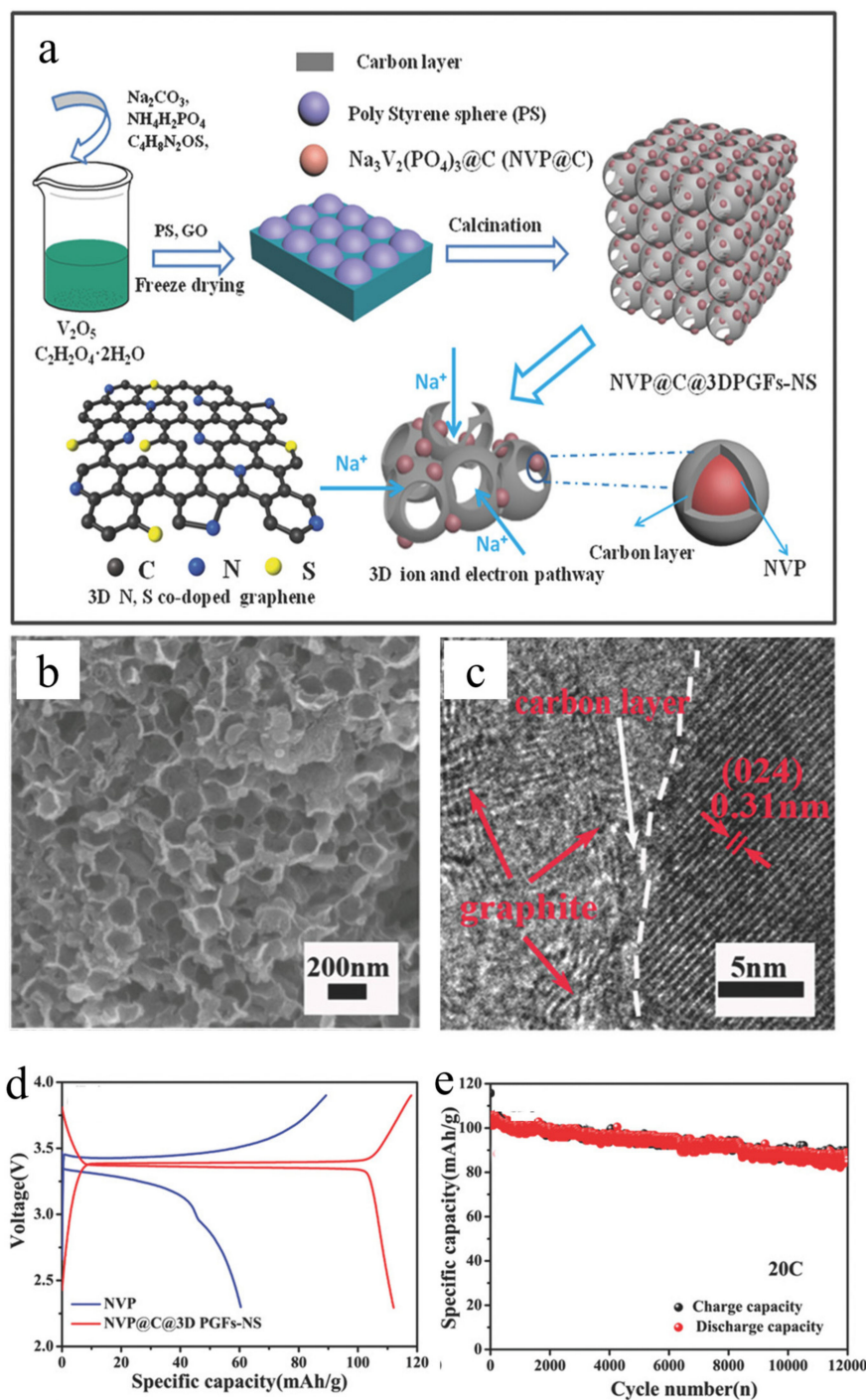

Figure 9. (**a**) Schematical synthesis of NVP@C@3DPGFs-NS, the (**b**) SEM image, (**c**) TEM image, (**d**) charge/discharge curves, and (**e**) cycling capability of NVP@C@3DPGFs-NS. Reprinted with permission from Ref. [92]. 2017, WILEY-VCH.

Table 3. Summary of NVP with different morphology for storage properties.

Composition	Morphology	Rate Performance	Cycle Number	Ref.
$Na_3V_2(PO_4)_3$@AC	Nanoparticle	5 C, 100.6 mAh/g	200	[44]
C@$Na_3V_2(PO_4)_3$@pC	Double-shell nanospheres	10 C, 103 mAh/g	1000	[60]
$Na_3V_2(PO_4)_3$-F/C	Nanofibers	C/10, 103 mAh/g	50	[76]
NVP@C@rGO	3D porous composites	1 C, 115 mAh/g	10,000	[78]
Graphene-bound NVP	3D continuous network	30 C, 71.9 mAh/g	1000	[79]
NVP/rGO HSs	Hollow spheres	1 C, 109 mAh/g	400	[80]
NVP@C+N@CNTs	Nanoparticle with CNTs	C/5, 86.5 mAh/g	400	[82]
NVP/CNT	Microsphere	10 C, 88.5 mAh/g	150	[83]
NVP/C@CNTs-WC	Nanoparticle with CNTs	50 C, 84.5 mAh/g	400	[84]
NVP@C	Double carbon-wrapped	1 C, 100 mAh/g	40	[85]
$Na_3V_2(PO_4)_3$@C@CMK-3	3D CMK-3	1 C, 115 mAh/g	2000	[87]
NVP/C-Ag	Particle	10 C, 95 mAh/g	500	[90]
NVP-NC	Particle	10 C, 94 mAh/g	600	[91]
$Na_3V_2(PO_4)_3$@C@3DPGFs-NS	3D porous composites	20 C, 86 mAh/g	12,000	[92]
$Na_3V_2(PO_4)_3$@C	3D nanofibers	10 C, 110 mAh/g	1000	[93]
$Na_3V_2(PO_4)_3$/CS	Core-sheath nanowires	1 C, 94 mAh/g	50	[94]
$Na_3V_2(PO_4)_3$@CNT-G	3D continuous free-standing foam	30 C, 109 mAh/g	2000	[95]
$Na_3V_2(PO_4)_3$@C	3D porous self-standing	C/2,110 mAh/g	2000	[96]
$Na_3V_2(PO_4)_3$@C-$B_{0.38}$	Nanoparticles	C/5, 87.1 mAh/g	50	[97]

4. Conclusions and Outlook

NVP has demonstrated great potential in SIBs as the cathode due to its high operating voltage, high ionic conductivity, and good structural and thermal stability. In this review, we briefly analyze various carbon coating strategies, such as graphene, carbon nanotubes, and other carbon allotropes, to improve the electronic conductivity of NVP towards high-performance SIBs. The results suggest that various carbons not only ameliorate the structure of NVP but also enhance the conductivity of the whole electrode. Meanwhile, the carbon matrix can store Na^+ by itself. Beyond that, heteroatom doping has also been employed to enhance the conductivity of pure NVP by increasing the carrier concentration. Despite the NVP cathode materials have developed rapidly in recent years, there are still some key issues that have to be resolved before the application of NVP on a large scale. Firstly, high-capacity NVP electrodes should be designed by involving multi-electron reactions. In this regard, the multi-scale computational models are necessarily put forward as a guide. Further, it is still a challenge to achieve high conductive NVP with excellent electrochemical properties. Fortunately, great efforts have been devoted to dope transition metal ions into NVP to improve the electronic conductivity from the inherent structure of the material, such as Mg^{2+} and Mn^{2+}, etc. On the other hand, the substitution of V sites by Hf, Zr, and W deserves to be explored as well. Finally, high voltage electrolyte is essential to achieve the multi-electron transfer of NVP cathodes and thus higher energy density.

Institutional Review Board Statement: Not applicable.

Informed Consent Statement: Not applicable.

Data Availability Statement: No new data were created or analyzed in this study. Data sharing does not apply to this article.

Conflicts of Interest: The authors declare no conflict of interest.

References

1. He, Z.; Jiang, Y.; Meng, W.; Zhu, J.; Liu, Y.; Dai, Y.; Wang, L.L. Advanced LiTi$_2$(PO$_4$)$_3$@N-doped carbon anode for aqueous lithium ion batteries. *Electrochim. Acta* **2016**, *222*, 1491–1500. [CrossRef]
2. Marom, R.; Amalraj, S.F.; Leifer, N.; Jacob, D.; Aurbach, D. A review of advanced and practical lithium battery materials. *J. Mater. Chem.* **2011**, *21*, 9938–9954. [CrossRef]
3. Goodenough, J.B.; Park, K.S. The Li-ion rechargeable battery: A perspective. *J. Am. Chem. Soc.* **2013**, *135*, 1167–1176. [CrossRef] [PubMed]

4. Li, Y.; Chen, Y.; Luo, L.; Ming, X.; Li, J.; Lei, T.; Deng, S.; Guo, J.; Zhu, J.; Chang, S. Surface in-situ reconstruction of $LiNi_{0.8}Co_{0.1}Mn_{0.1}O_2$ cathode materials interacting with antimony compounds and the electrochemical performances. *J. Electroanal. Chem.* **2019**, *854*, 113582. [CrossRef]

5. Cao, X.; Sun, Q.; Zhu, L.; Xie, L. $Na_3V_2(PO_4)_3$ nanoparticles confined in functional carbon framework towards high-rate and ultralong-life sodium storage. *J. Alloys Compd.* **2019**, *791*, 296–306. [CrossRef]

6. Yi, H.; Lin, L.; Ling, M.; Lv, Z.; Li, R.; Fu, Q.; Zhang, H.; Zheng, Q.; Li, X. Scalable and economic synthesis of high-performance $Na_3V_2(PO_4)_2F_3$ by a solvothermal-ball-milling method. *ACS Energy Lett.* **2019**, *4*, 1565–1571. [CrossRef]

7. Liu, T.; Zhang, Y.; Jiang, Z.; Zeng, X.; Ji, J.; Li, Z.; Gao, X.; Sun, M.; Lin, Z.; Ling, M.; et al. Exploring competitive features of stationary sodium ion batteries for electrochemical energy storage. *Energy Environ. Sci.* **2019**, *12*, 1512–1533. [CrossRef]

8. Zhang, B.W.; Ma, K.X.; Lv, X.; Shi, K.; Wang, Y.; Nian, Z.Y.; Li, Y.H.; Wang, L.; Dai, L.; He, Z.X. Recent advances of NASICON-$Na_3V_2(PO_4)_3$ as cathode for sodium-ion batteries: Synthesis, modifications, and perspectives. *J. Alloys Compd.* **2021**, *867*, 159060. [CrossRef]

9. Chagas, L.G.; Jeong, S.; Hasa, I.; Passerini, S. Ionic liquid-based electrolytes for sodium-ion batteries: Tuning properties to enhance the electrochemical performance of manganese-based layered oxide cathode. *ACS Appl. Mater. Inter.* **2019**, *11*, 22278–22289. [CrossRef]

10. Gu, Y.; Xiao, F.; Xu, K.; Pan, X.; Li, J.; Xu, C.; Zhou, X. Outstanding electrochemical performance of sodium vanadium phosphate cathode co-modified by carbon-coating and titanium-doping for Na-ion batteries. *Ceram. Int.* **2019**, *45*, 12570–12574. [CrossRef]

11. Zhao, J.; Gao, Y.; Liu, Q.; Meng, X.; Chen, N.; Wang, C.; Du, F.; Chen, G. High rate capability and enhanced cyclability of $Na_3V_2(PO_4)_2F_3$ cathode by in situ coating of carbon nanofibers for sodium-ion battery applications. *Chem. Eur. J.* **2018**, *24*, 2913–2919. [CrossRef] [PubMed]

12. Slater, M.D.; Kim, D.; Lee, E.; Johnson, C.S. Sodium-ion batteries. *Adv. Funct. Mater.* **2013**, *23*, 947–958. [CrossRef]

13. Kim, S.W.; Seo, D.H.; Ma, X.; Ceder, G.; Kang, K. Electrode materials for rechargeable sodium-ion batteries: Potential alternatives to current lithium-ion batteries. *Adv. Energy Mater.* **2012**, *2*, 710. [CrossRef]

14. Zhou, Y.X.; Zhang, L.L.; Yang, X.L.; Huang, Y.H.; Ding, X.K.; Ma, D.; Wang, J.Q. Synthesis of nanosheet-structured $Na_3V_2(PO_4)_3/C$ as high-performance cathode material for sodium ion batteries using anthracite as carbon source. *Ceram. Int.* **2017**, *43*, 2333. [CrossRef]

15. Khan, Z.; Vagin, M.; Crispin, X. Can hybrid Na–air batteries outperform nonaqueous Na–O_2 batteries? *Adv. Sci.* **2020**, *7*, 1902866. [CrossRef]

16. Zhao, Y.; Yang, D.; He, T.; Li, J.; Wei, L.; Wang, D.; Wang, Y.; Wang, X.; Chen, G.; Wei, Y. Vacancy engineering in VS_2 nanosheets for ultrafast pseudocapacitive sodium ionstorage. *Chem. Eng. J.* **2021**, *421*, 129715. [CrossRef]

17. Lv, Z.Q.; Ling, M.X.; Yue, M.; Li, X.F.; Song, M.M.; Zheng, Q.; Zhang, H.M. Vanadium-based polyanionic compounds as cathode materials for sodium-ion batteries: Toward high-energy and high-power applications. *J. Energy Chem.* **2021**, *55*, 361–390. [CrossRef]

18. Chen, S.; Wu, C.; Shen, L.; Zhu, C.; Huang, Y.; Xi, K.; Maier, J.; Yu, Y. Challenges and Perspectives for NASICON-Type Electrode Materials for Advanced Sodium-Ion Batteries. *Adv. Mater.* **2017**, *29*, 1700431. [CrossRef]

19. Takeda, Y.; Nakahara, K.; Nishijima, M.; Imanishi, N.; Yamamoto, O.; Takano, M.; Kanno, R. Crystal chemistry and physical properties of $La_{2-x}Sr_xNiO_4$ ($0 \leq x \leq 1.6$). *Mater. Res. Bull.* **1990**, *25*, 293–306. [CrossRef]

20. Ma, X.; Chen, H.; Ceder, G. Electrochemical properties of monoclinic $NaMnO_2$. *J. Electrochem. Soc.* **2011**, *158*, A1307. [CrossRef]

21. Komaba, S.; Takei, C.; Nakayama Ogata, T.A.; Yabuuchi, N. Electrochemical intercalation activity of layered $NaCrO_2$ vs. $LiCrO_2$. *Electrochem. Commun.* **2010**, *12*, 355. [CrossRef]

22. Hamani, D.; Ati, M.; Tarascon, J.M.; Rozier, P. Na_xVO_2 as possible electrode for Na-ion batteries. *Electrochem. Commun.* **2011**, *13*, 938. [CrossRef]

23. Recham, N.; Chotard, J.N.; Dupont, L.; Djell, K.; Armand, M.; Tarasconz, J.M. Ionothermal synthesis of sodium-based fluorophosphate cathode materials. *J. Electrochem. Soc.* **2009**, *156*, A993. [CrossRef]

24. Pu, X.J.; Wang, H.M.; Yuan, T.C.; Cao, S.N.; Liu, S.Y.; Xu, L.; Yang, H.X.; Ai, X.P.; Chen, Z.X.; Cao, Y.L. $Na_4Fe_3(PO_4)_2P_2O_7/C$ nanospheres as low-cost, high-performance cathode material for sodium-ion batteries. *Energy Stor. Mater.* **2019**, *22*, 330–336. [CrossRef]

25. Rajagopalan, R.; Chen, B.; Zhang, Z.; Wu, X.L.; Du, Y.; Huang, Y.; Li, B.; Zong, Y.; Wang, J.; Nam, G.H.; et al. Improved Reversibility of Fe^{3+}/Fe^{4+} Redox Couple in Sodium Super Ion Conductor Type $Na_3Fe_2(PO_4)_3$ for Sodium-Ion Batteries. *Adv. Mater.* **2017**, *29*, 1605694. [CrossRef]

26. Xia, X.; Cao, Y.; Yao, L.; Yang, H.; Zhang, J. MCNT-Reinforced $Na_3Fe_2(PO_4)_3$ as Cathode Material for Sodium-Ion Batteries. *Arab J. Sci. Eng.* **2020**, *45*, 143–151. [CrossRef]

27. Piernas Muñoz, M.J.; Martínez, E.C. *Prussian Blue Based Batteries*; Springer: Cham, Switzerland, 2018; pp. 9–22.

28. Qian, J.; Wu, C.; Cao, Y.; Ma, Z.; Huang, Y.; Ai, X.; Yang, H. Prussian blue cathode materials for sodium-ion batteries and other ion batteries. *Adv. Energy Mater.* **2018**, *8*, 1702619. [CrossRef]

29. You, Y.; Wu, X.L.; Yin, Y.X.; Guo, Y.-G. High-quality Prussian blue crystals as superior cathode materials for room-temperature sodium-ion batteries. *Energy Environ. Sci.* **2014**, *7*, 1643. [CrossRef]

30. Wang, B.; Han, Y.; Wang, X.; Bahlawane, N.; Pan, H.; Yan, M.; Jiang, Y. Prussian blue analogs for rechargeable batteries. *Iscience* **2018**, *3*, 110. [CrossRef]

31. Fernández, N.; Sánchez-Fontecoba, P.; Castillo-Martínez, E.; Carretero-González, J.; Rojo, T.; Armand, M. Polymeric redox-active electrodes for sodium-ion batteries. *Chem. Sus. Chem.* **2018**, *11*, 311–319. [CrossRef]

32. Mendiboure, A.; Delmas, C.; Hagenmuller, P. Electrochemical intercalation and deintercalation of Na_xMnO_2 bronzes. *J. Solid State Chem.* **1985**, *57*, 323–331. [CrossRef]

33. Manikandan, P.; Heo, S.; Kim, H.W.; Jeong, H.Y.; Lee, E.; Kim, Y. Structural characterization of layered $Na_{0.5}Co_{0.5}Mn_{0.5}O_2$ material as a promising cathode for sodium-ion batteries. *J. Power Source* **2017**, *80*, 442–449. [CrossRef]

34. Komaba, S.; Yabuuchi, N.; Nakayama, T.; Ogata, A.; Ishikawa, T.; Nakai, I. Study on the reversible electrode reaction of $Na_{1-x}Ni_{0.5}Mn_{0.5}O_2$ for a rechargeable sodium-ion battery. *Inorg. Chem.* **2012**, *51*, 6211–6220. [CrossRef] [PubMed]

35. Han, D.W.; Ku, J.H.; Kim, R.H.; Yun, D.J.; Lee, S.S.; Doo, S.G. Aluminum manganese oxides with mixed crystal structure: High-energy-density cathodes for rechargeable sodium batteries. *Chem. Sus. Chem.* **2014**, *7*, 1870–1875. [CrossRef] [PubMed]

36. Sun, J.; Shen, J.; Wang, T. Electrochemical study of $Na_{0.66}Ni_{0.33}Mn_{0.67}-xMo_xO_2$ as cathode material for sodium-ion battery. *J. Alloys Compd.* **2017**, *709*, 481–486. [CrossRef]

37. Ding, F.X.; Zhao, C.L.; Zhou, D.; Meng, Q.S.; Xiao, D.D.; Zhang, Q.Q.; Niu, Y.S.; Li, Y.Q.; Rong, X.H.; Lu, Y.X.; et al. A Novel Ni-rich O3-Na[$Ni_{0.60}Fe_{0.25}Mn_{0.15}$]$O_2$ Cathode for Na-ion Batteries. *Energy Storage Mater.* **2020**, *30*, 420–430. [CrossRef]

38. Fang, Y.J.; Yu, X.Y.; Xiong, W.L. A practical high-energy cathode for sodium-ion batteries based on uniform P2-$Na_{0.7}CoO_2$ microspheres. *Angew. Chem. Int. Ed.* **2017**, *21*, 5801–5805. [CrossRef]

39. Wang, L.; Song, J.; Qiao, R.M.; Wray, L.A.; Hossain, M.A.; Chuang, Y.D.; Yang, W.L.; Lu, Y.H.; Evans, D. Rhombohedral Prussian White as Cathode for Rechargeable Sodium-Ion Batteries. *J. Am. Chem. Soc.* **2015**, *137*, 2548–2554. [CrossRef]

40. Hwang, J.; Kim, J. A supercritical methanol route for the synthesis of sodium iron oxide submicron plates for use as a cathode material for sodium-ion batteries. *Mater. Lett.* **2017**, *206*, 100–104. [CrossRef]

41. Zhou, D.; Huang, W.; Lv, X.; Zhao, F. A novel P2/O3 bi phase $Na_{0.67}Fe_{0.425}Mn_{0.425}Mg_{0.15}O_2$ as cathode for high-performance sodium-ion batteries. *J. Power Source* **2019**, *421*, 147–155. [CrossRef]

42. Li, A.H.; Feng, Z.Y.; Sun, Y.; Shang, L.M.; Xu, L.Q. Porous organic polymer/RGO composite as high performance cathode for half and full sodium ion batteries. *J. Power Source* **2017**, *343*, 424–430. [CrossRef]

43. Luo, C.; Fan, X.L.; Ma, Z.H.; Gao, T.; Wang, C.S. Self-Healing Chemistry between Organic Material and Binder for Stable Sodium-Ion Batteries. *Chem* **2017**, *3*, 1050–1062. [CrossRef]

44. Li, J.; Chen, Y.; Zhou, T.; Shi, H.; Zheng, Z.; Wang, Y.; Guo, L. Dual-carbon coated $Na_3V_2(PO_4)_3$ derived from reduced graphene oxide and nanocellulose with porous structure for high performance sodium-ion batteries. *Appl. Surf. Sci.* **2023**, *610*, 155553. [CrossRef]

45. Li, H.; Chen, X.; Jin, T.; Bao, W.; Zhang, Z.; Jiao, L. Robust graphene layer modified $Na_2MnP_2O_7$ as a durable high-rate and high energy cathode for Na-ion batteries. *Energy Storage Mater.* **2019**, *16*, 383–390. [CrossRef]

46. Zaghib, K.; Julien, C.M. Structure and electrochemistry of $FePO_4 \cdot 2H_2O$ hydrate. *J. Power Source* **2005**, *142*, 279–284. [CrossRef]

47. Karami, H.; Taala, F. Synthesis, characterization and application of $Li_3Fe_2(PO_4)_3$ nanoparticles as cathode of lithium-ion rechargeable batteries. *J. Power Source* **2011**, *196*, 6400–6411. [CrossRef]

48. Yin, Y.; Hu, Y.; Wu, P.; Zhang, H.; Cai, C. A graphene-amorphous $FePO_4$ hollow nanosphere hybrid as a cathode material for lithium ion batteries. *Chem. Commun.* **2012**, *48*, 2137–2139. [CrossRef]

49. Guo, B.; Ruan, H.; Zheng, C.; Fei, H.; Wei, M. Hierarchical $LiFePO_4$ with a controllable growth of the (010) facet for lithiumion batteries. *Sci. Rep.* **2013**, *3*, 2788–2793. [CrossRef]

50. Zhang, S.M.; Zhang, J.X.; Xu, S.J.; Yuan, X.J.; Tan, T. Synthesis, morphological analysis and electrochemical performance of iron hydroxyl phosphate as a cathode material for lithium ion batteries. *J. Power Source* **2013**, *243*, 274–279. [CrossRef]

51. Pu, X.; Wang, H.; Zhao, D.; Yang, H.; Ai, X.; Cao, S.; Chen, Z.; Cao, Y. Recent progress in rechargeable sodium-ion batteries: Toward high-power applications. *Small* **2019**, *15*, 1805427. [CrossRef]

52. Niu, Y.; Zhang, Y.; Xu, M. A review on pyrophosphate framework cathode materials for sodium-ion batteries. *J. Mater. Chem. A* **2019**, *7*, 15006–15025. [CrossRef]

53. Guo, S.P.; Li, J.C.; Xu, Q.T.; Ma, Z.; Xue, H.G. Recent achievements on polyanion-type compounds for sodium-ion batteries: Syntheses, crystal chemistry and electrochemical performance. *J. Power Source* **2017**, *361*, 285–299. [CrossRef]

54. Wang, X.; Wang, W.; Zhu, B.; Qian, F.; Fang, Z. Mo-doped $Na_3V_2(PO_4)_3$@C composites for high stable sodium ion battery cathode. *Front. Mater. Sci.* **2018**, *12*, 53–63. [CrossRef]

55. Li, X.; Huang, Y.; Wang, J.; Miao, L.; Li, Y.; Liu, Y.; Qiu, Y.; Fang, C.; Han, J.; Huang, Y. High valence Mo-doped $Na_3V_2(PO_4)_3$/C as a high rate and stable cycle-life cathode for sodium battery. *J. Mater. Chem. A* **2018**, *6*, 1390–1396. [CrossRef]

56. Zhu, Q.; Wang, M.; Nan, B.; Shi, H.; Zhang, X.; Deng, Y.; Wang, L.; Chen, Q.; Lu, Z. Core/shell nanostructured $Na_3V_2(PO_4)_3$/C/TiO_2 composite nanofibers as a stable anode for sodium-ion batteries. *J. Power Source* **2017**, *362*, 147–159. [CrossRef]

57. Zheng, W.; Huang, X.; Ren, Y.; Wang, H.; Zhou, S.; Chen, Y.; Ding, X.; Zhou, T. Porous spherical $Na_3V_2(PO_4)_3$/C composites synthesized via a spray drying-assisted process with high-rate performance as cathode materials for sodium-ion batteries. *Solid State Ion.* **2017**, *308*, 161–166. [CrossRef]

58. Li, G.; Jiang, D.; Wang, H.; Lan, X.; Zhong, H.; Jiang, Y. Glucose-assisted synthesis of $Na_3V_2(PO_4)_3$ composite as an electrode material for high-performance sodium-ion batteries. *J. Power Source* **2014**, *265*, 325–334. [CrossRef]

59. Tao, S.; Cui, P.X.; Huang, W.F.; Yu, Z.; Wang, X.B.; Wei, S.H.; Liu, D.B.; Song, L.; Chu, W.S. Sol-gel design strategy for embedded Na$_3$V$_2$(PO$_4$)$_3$ particles into carbon matrices for high-performance sodium-ion batteries. *Carbon* **2016**, *96*, 1028–1033. [CrossRef]

60. Zhu, C.B.; Song, K.P.; Aken, P.A.; Maier, V.J.; Yu, Y. Carbon-coated Na$_3$V$_2$(PO$_4$)$_3$ embedded in porous carbon matrix: An ultrafast Na-storage cathode with the potential of outperforming Li cathodes. *Nano Lett.* **2014**, *14*, 2175–2180. [CrossRef]

61. Li, S.; Dong, Y.F.; Xu, L.; Xu, X.; He, L.; Mai, L.Q. Effect of carbon matrix dimensions on the electrochemical properties of Na3V$_2$(PO$_4$)$_3$ nanograins for high-performance symmetric sodium-ion batteries. *Adv. Mater.* **2014**, *26*, 3358–3363. [CrossRef]

62. Zhu, X.M.; Fang, Y.J.; Ai, X.P.; Yang, H.X.; Cao, Y.L. Na$_3$V$_2$(PO$_4$)$_3$/C nanocomposite synthesize via pre-reduction process as high-performance cathode material for sodium-ion batteries. *J. Alloys Compd.* **2015**, *646*, 170–174. [CrossRef]

63. Jian, Z.L.; Zhao, L.; Pan, H.L.; Hu, Y.S.; Li, H.; Chen, W.; Chen, L.Q. Carbon coated Na$_3$V$_2$(PO$_4$)$_3$ as novel electrode material for sodium ion batteries. *Electrochem. Commun.* **2012**, *14*, 86–89. [CrossRef]

64. Cheng, D.; Li, Y.; Zhang, J.; Tian, M.; Wang, B.; He, Z.; Dai, L.; Wang, L. Recent advances in electrospun carbon fiber electrode for vanadium redox flow battery: Properties, structures, and perspectives. *Carbon* **2020**, *170*, 527–542. [CrossRef]

65. Jiang, Y.; Zeng, L.; Wang, J.; Li, W.; Pana, F.; Yu, Y. A carbon coated NASICON structure material embedded in porous carbon enabling superior sodium storage performance: NaTi$_2$(PO$_4$)$_3$ as an example. *Nanoscale* **2015**, *7*, 14723. [CrossRef] [PubMed]

66. Zhang, Q.; Wang, W.; Wang, Y.; Feng, P.; Wang, K.; Cheng, S.; Jiang, K. Controllable construction of 3D-skeleton-carbon coated Na$_3$V$_2$(PO$_4$)$_3$ for high-performance sodium ion battery cathode. *Nano Energy* **2016**, *20*, 11. [CrossRef]

67. Fang, J.; Wang, S.; Li, Z.; Chen, H.; Xia, L.; Ding, L.; Wang, H. Porous Na$_3$V$_2$ (PO$_4$)$_3$@C nanoparticles enwrapped in three-dimensional graphene for high performance sodium-ion batteries. *J. Mater. Chem. A* **2016**, *4*, 1180. [CrossRef]

68. Li, H.; Yu, X.; Bai, Y.; Wu, F.; Wu, C.; Liu, L.Y.; Yang, X.Q. Effects of Mg doping on the remarkably enhanced electrochemical performance of Na$_3$V$_2$(PO$_4$)$_3$ cathode materials for sodium ion batteries. *J. Mater. Chem. A* **2015**, *3*, 9578. [CrossRef]

69. Aragón, M.J.; Lavela, P.; Alcántara, R.; Tirado, J.L. Effect of aluminum doping on carbon loaded Na$_3$V$_2$(PO$_4$)$_3$ as cathode material for sodium-ion batteries. *Electrochim. Acta* **2015**, *180*, 824. [CrossRef]

70. Zhu, C.; Kopold, P.; van Aken, P.A.; Maier, J.; Yu, Y. High power-high energy sodium battery based on threefold interpenetrating network. *Adv. Mater.* **2016**, *28*, 2409. [CrossRef]

71. Song, W.; Ji, X.; Wu, Z.; Zhu, Y.; Yang, Y.; Chen, J.; Jing, M.; Li, F.; Banks, C.E. First exploration of Na-ion migration pathways in the NASICON structure Na$_3$V$_2$(PO$_4$)$_3$. *J. Mater. Chem. A* **2014**, *2*, 5358. [CrossRef]

72. Xiao, H.; Huang, X.; Ren, Y.; Wang, H.; Ding, J.; Zhou, S.; Ding, X.; Chen, Y. Enhanced sodium ion storage performance of Na$_3$V$_2$(PO$_4$)$_3$ with N-doped carbon by folic acid as carbon-nitrogen source. *J. Alloys Compd.* **2018**, *732*, 454–459. [CrossRef]

73. Klee, R.; Aragon, M.J.; Lavela, P.; Alcantara, R.; Tirado, J.L. Na$_3$V$_2$(PO$_4$)$_3$/C nanorods with improved electrode-electrolyte interface as cathode material for sodium-ion batteries. *ACS Appl. Mater. Interfaces* **2016**, *8*, 23151–23159. [CrossRef] [PubMed]

74. Lim, S.Y.; Kim, H.; Shakoor, R.A.; Jung, Y.; Choi, J.W. Electrochemical and Thermal Properties of NASICON Structured Na$_3$V$_2$(PO$_4$)$_3$ as a Sodium Rechargeable Battery Cathode: A Combined Experimental and Theoretical Study. *J. Electrochem. Soc.* **2012**, *159*, A1393–A1397. [CrossRef]

75. Bianchini, M.; Fauth, F.; Brisset, N.; Weill, F.; Masquelier, E.; Croguennec, L. Comprehensive investigation of the Na$_3$V$_2$(PO$_4$)$_2$F$_3$–NaV$_2$(PO$_4$)$_2$F$_3$ system by operando high resolution synchrotron X-ray diffraction. *Chem. Mater.* **2015**, *27*, 3009–3020. [CrossRef]

76. Liu, J.; Tang, K.; Song, K.; van Aken, P.A.; Yu, Y.; Maier, J. Electrospun Na$_3$V$_2$(PO$_4$)$_3$/C nanofibers as stable cathode materials for sodium-ion batteries. *Nanoscale* **2014**, *6*, 5081–5086. [CrossRef]

77. Xiao, H.; Huang, X.; Ren, Y.; Ding, X.; Chen, Y.; Zhou, S. Improved electrochemical performance of Na$_3$V$_2$(PO$_4$)$_3$ modified by N-doped carbon coating and Zr doping. *Solid State Ion.* **2019**, *333*, 93–100. [CrossRef]

78. Rui, X.; Sun, W.; Wu, C.; Yu, Y.; Yan, Q. An Advanced Sodium-Ion Battery Composed of Carbon Coated Na$_3$V$_2$(PO$_4$)$_3$ in a Porous Graphene Network. *Adv. Mater.* **2015**, *27*, 6670–6676. [CrossRef]

79. Chang, X.Q.; Zhu, Q.Z.; Sun, N.; Guan, Y.B.; Wang, R.; Zhao, J.H.; Feng, M.Y.; Xu, B. Graphene-bound Na$_3$V$_2$(PO$_4$)$_3$ film electrode with excellent cycle and rate performance for Na-ion batteries. *Electrochim. Acta* **2018**, *296*, 282–290. [CrossRef]

80. Xu, J.Y.; Gu, E.L.; Zhang, Z.Z.; Xu, Z.H.; Xu, Y.F.; Du, Y.C.; Zhu, X.S.; Zhou, X.S. Fabrication of porous Na$_3$V$_2$(PO$_4$)$_3$/reduced graphene oxide hollow spheres with enhanced sodium storage performance. *J. Colloid Interface Sci.* **2020**, *567*, 84–91. [CrossRef]

81. Xu, Y.N.; Wei, Q.L.; Xu, C.; Li, Q.D.; An, Q.Y.; Zhang, P.F.; Sheng, J.Z.; Zhou, L.; Mai, L.Q. Layer-by-Layer Na$_3$V$_2$(PO$_4$)$_3$ Embedded in Reduced Graphene Oxide as Superior Rate and Ultralong-Life Sodium-Ion Battery Cathode. *Adv. Energy Mater.* **2016**, *6*, 1600389. [CrossRef]

82. Shen, W.; Li, H.; Guo, Z.; Wang, C.; Li, Z.; Xu, Q.; Liu, H.; Wang, Y.; Xia, Y. Double-Nanocarbon Synergistically Modified Na$_3$V$_2$(PO$_4$)$_3$: An Advanced Cathode for High-Rate and Long-Life Sodium-Ion Batteries. *ACS Appl. Mater. Interfaces* **2016**, *8*, 15341–15351. [CrossRef] [PubMed]

83. Chen, H.; Zhang, B.; Wang, X.; Dong, P.; Tong, H.; Zheng, J.C.; Yu, W.; Zhang, J. CNT-Decorated Na$_3$V$_2$(PO$_4$)$_3$ Microspheres as a High-Rate and Cycle-Stable Cathode Material for Sodium Ion Batteries. *ACS Appl. Mater. Interfaces* **2018**, *10*, 3590–3595. [CrossRef] [PubMed]

84. Sun, S.Q.; Chen, Y.J.; Cheng, J.; Tian, Z.Y.; Wang, C.; Wu, G.P.; Liu, C.C.; Wang, Y.Z.; Li, G. Constructing dimensional gradient structure of Na$_3$V$_2$(PO$_4$)$_3$/C@CNTs-WC by wolfram substitution for superior sodium storage. *Chem. Eng. J.* **2021**, *420*, 130453. [CrossRef]

85. Duan, W.C.; Zhu, Z.Q.; Li, H.; Hu, Z.; Zhang, K.; Cheng, F.Y.; Chen, J. Na$_3$V$_2$(PO$_4$)$_3$@C core–shell nanocomposites for rechargeable sodium-ion batteries. *J. Mater. Chem. A* **2014**, *2*, 8668. [CrossRef]

86. Li, S.J.; Ge, P.; Zhang, C.T.; Sun, W.; Hou, H.S.; Ji, X.B. The electrochemical exploration of double carbon-wrapped $Na_3V_2(PO_4)_3$: Towards long-time cycling and superior rate sodium-ion battery cathode. *J. Power Source* **2017**, *366*, 249–258. [CrossRef]

87. Jiang, Y.; Yang, Z.; Li, W.; Zeng, L.; Pan, F.; Wang, M.; Wei, X.; Hu, G.; Gu, L.; Yu, Y. Nanoconfined Carbon-Coated $Na_3V_2(PO_4)_3$ Particles in Mesoporous Carbon Enabling Ultralong Cycle Life for Sodium-Ion Batteries. *Adv. Energy Mater.* **2015**, *5*, 1402104. [CrossRef]

88. Wang, G.; Liu, H.; Liu, J.; Qiao, S.; Lu, G.M.; Munroe, P.; Ahn, H. Mesoporous $LiFePO_4$/C Nanocomposite Cathode Materials for High Power Lithium Ion Batteries with Superior Performance. *Adv. Mater.* **2010**, *22*, 4944. [CrossRef]

89. Zhang, H.; Tao, H.; Jiang, Y.; Jiao, Z.; Wu, M.; Zhao, B. Ordered CoO/CMK-3 nanocomposites as the anode materials for lithium-ion batteries. *J. Power Source* **2010**, *195*, 2950–2955. [CrossRef]

90. Hong, X.D.; Huang, X.B.; Ren, Y.R.; Wang, H.Y.; Ding, X.; Jin, J.L. Superior Na-storage performance of $Na_3V_2(PO_4)_3$/C-Ag composites as cathode material for Na-ion battery. *J. Alloys Compd.* **2020**, *822*, 153587. [CrossRef]

91. Wang, Y.P.; Zhao, K.J.; Wang, k.; Li, H.H.; Jiang, H.B.; Chen, L. N-doped carbon confined $Na_3V_2(PO_4)_3$ derived from an organophosphonic acid as a high-performance cathode for sodium-ion batteries. *J. Alloys Compd.* **2020**, *844*, 156118. [CrossRef]

92. Jiang, Y.; Wu, Y.; Chen, Y.; Qi, Z.; Shi, J.; Gu, L.; Yu, Y. Design Nitrogen (N) and Sulfur (S) co-Doped 3D Graphene Network Architectures for High-Performance Sodium Storage. *Small* **2018**, *14*, 1703471. [CrossRef] [PubMed]

93. Ren, W.H.; Yao, X.H.; Niu, C.J.; Zheng, Z.P.; Zhao, K.N.; An, Q.Y.; Wei, Q.L.; Yan, M.Y.; Zhang, L.; Mai, L.Q. Cathodic polarization suppressed sodium-ion full cell with a 3.3 V high-voltage. *Nano Energy* **2016**, *28*, 216–223. [CrossRef]

94. Kajiyama, S.; Kikkawa, J.; Hoshino, J.; Okubo, M.; Hosono, E. Assembly of $Na_3V_2(PO_4)_3$ Nanoparticles Confined in a One-Dimensional Carbon Sheath for Enhanced Sodium-Ion Cathode Properties. *Chem. Eur. J.* **2014**, *20*, 12636–12640. [CrossRef] [PubMed]

95. Shen, W.; Wang, C.; Xu, Q.J.; Liu, H.M.; Wang, Y.G. Nitrogen-Doping-Induced Defects of a Carbon Coating Layer Facilitate Na-Storage in Electrode Materials. *Adv. Energy Mater.* **2015**, *5*, 1400982. [CrossRef]

96. Yi, H.M.; Li, D.; Lv, Z.Q.; Li, R.; Ling, M.; Zhang, H.; Zheng, Q.; Li, X. Constructing high-performance 3D porous self-standing electrodes with various morphologies and shapes by a flexible phase separation-derived method. *J. Mater. Chem. A* **2019**, *7*, 22550–22558. [CrossRef]

97. Shen, W.; Li, H.; Wang, C.; Li, Z.H.; Xu, Q.J.; Liu, H.M.; Wang, Y.G. Improved electrochemical performance of the $Na_3V_2(PO_4)_3$ cathode by B-doping of the carbon coating layer for sodium-ion batteries. *J. Mater. Chem. A* **2015**, *3*, 15190–15201. [CrossRef]